76-266

Attitude Stability of a Pseudorate Jet-Controlled Flexible Spacecraft

R.A. Millar* and F.R. Vigneron†
Communications Research Center, Ottawa, Canada

The small-angle stability of a single-axis spacecraft attitude control system incorporating a nonlinear pseudorate controller, jet actuator, flexible vehicle dynamics, and a loop time delay is analyzed. The dynamics include a low-frequency rigid vehicle mode and a highly underdamped flexible mode that has its modal frequency outside the rigid vehicle control system bandwidth. The single input sinusoidal describing function for the pseudorate controller is derived and used to determine the effect of the controller on each mode individually. A stable limit cycle for the rigid vehicle mode response is predicted. The flexible mode response is predicted to be stable, unstable, or to exhibit a stable limit cycle, depending on the loop time delay and the flexible mode frequency and damping. Simulation results verify the integrity and interpretation of analytically predicted stability conditions.

Introduction

IN this paper, the small angle (near deadband) stability of the attitude control system shown in Fig. 1 is analyzed. The system consists of a single-axis structurally flexible spacecraft, an attitude sensor, and a pseudorate controller. The problem stems from a requirement to understand basic relationships that govern the pseudorate attitude control of the Communications Technology Satellite (CTS),[1,2] also referred to as Hermes. The results and technique presented are applicable to the CTS and are expected to find application in the design and analysis of similar spacecraft, which employ pseudorate attitude controllers and whose dynamics are amenable to a modal transfer function representation such as that shown in Fig. 1.

In this class of spacecraft, the initial control system synthesis and sizing of the pseudorate parameters are based on the premise that the spacecraft basically behaves as a rigid body. The controller design is such that the structural frequencies are somewhat higher than the control system bandwidth. Structural flexibility cannot be ignored, however, because of the highly underdamped nature of the flexible modes, the presence of a loop time delay comparable with the flexible mode oscillation periods, and the fact that the attitide sensor detects not only the low-frequency rigid vehicle motion but also the higher-frequency structural modes of deformation.

The nonlinear nature of the controller, the inclusion of structural flexibility, and a loop time delay preclude rigorous analysis of the system shown in Fig. 1. In the following analysis, 1) the dual time constant pseudorate controller is replaced by its single input sinusoidal describing function; and 2) the effect of the controller on the stability of each dynamic mode indicated in the spacecraft dynamics block of Fig. 1 is analyzed separately, a simplification often invoked when modes are well separated in frequency (mode separability[3-6]). The approach reveals many of the basic functional relationships involved in pseudorate control of flexible spacecraft. Detailed simulation results of the complete system (Fig. 1) illustrate and verify the integrity and interpretation of the analytical results. Parameter values utilized are characteristic of the offset pseudorate controller and the roll dynamics of the CTS.

Presented as Paper 76-266 at the AIAA/CASI 6th Communcations Satellite Systems Conference, Montreal, Canada, April 5-8, 1976; received Sept. 26, 1977; revision received May 8, 1978.

Index category: Guidance and Control.

*Research Engineer, Department of Communications.

†Research Scientist, Department of Communications. Member AIAA.

System Description

The system (Fig. 1) incorporates a standard dual time constant pseudorate controller, a pair of thrusters, flexible spacecraft dynamics, and an attitude sensor. The controller consists of a dual time constant [τ_0 when $y(t) = \pm 1$, τ_f when $y(t) = 0$] feedback lag network (gain $K_f D$) around an on-off relay with deadband D and hysteresis H. The thrusters have a thrust level F and a moment arm L. The spacecraft dynamics include the rigid vehicle mode (zero frequency, zero damping) and a single highly underdamped fundamental flexible mode, which has a natural (unconstrained) modal frequency ω_l. The modal gain k_l is approximately equal to the inertia ratio of the flexible parts to the rigid parts.[7] The total spacecraft inertial (rigid plus flexible parts) is denoted by I. Associated with the attitude sensor is a gain K. A composite loop time delay T accounts for delays associated with the sensor and processing delays associated with the hardware implementation of the controller.

In accordance with standard design considerations such as those described in Ref. 8 (D determined by sensor noise level and pointing accuracy requirements, pseudorate saturation angle ϕ_s determined by large-angle capture requirements, minimum pseudorate on-time $\Delta t_{\min} \simeq H\tau_0/K_f D$ determined by limit cycle frequency considerations and thruster pneumatic response characteristics), the pseudorate parameters have the following characteristics:

$$H/D < 1 \tag{1a}$$

$$\tau_0 \ll \tau_f \tag{1b}$$

$$\phi_s \simeq K_f D \gg D, H \tag{1c}$$

$$\Delta t_{\min} \ll \tau_0, \tau_f \tag{1d}$$

$$\omega_b \simeq 1/\tau_f \tag{1e}$$

where ω_b is the rigid vehicle ($k_l = 0$) closed-loop system bandwidth. The bandwidth is based on the small signal attitude (position) and rate gain representation of the pseudorate described in Ref. 8. [Equation (1e) is obtained by setting $\rho = 0.5$ in Eq. (33) of Ref. 8.] The bandwidth has been

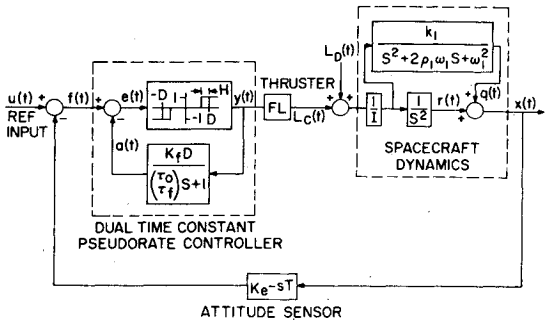

Fig. 1 Pseudorate attitude control of a flexible spacecraft.

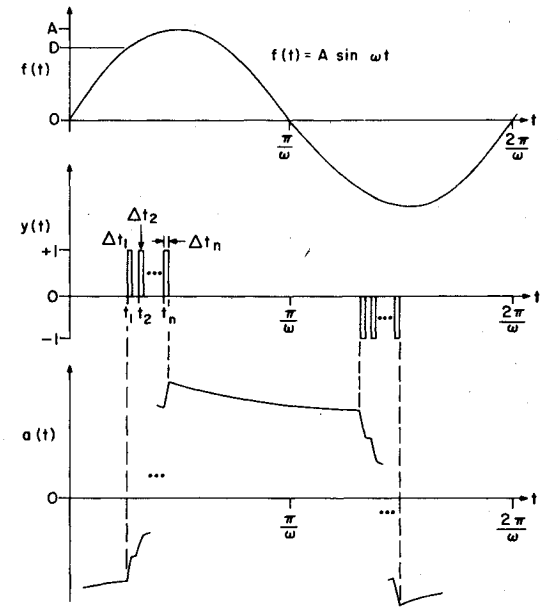

Fig. 2 Pseudorate sinusoidal response waveforms.

chosen such that

$$\omega_b \ll \omega_1 \tag{1f}$$

where ω_1 is the fundamental flexible mode frequency. The dual time constant feature allows ω_b and $\Delta t_{\min}$ to be chosen independently.

For input amplitude A near the deadband, i.e., when

$$A/D < \sim 5 \tag{2a}$$

the pseudorate on-times (thrust durations) are given approximately by the pseudorate minimum on-time $\Delta t_{\min}$ [see Eq. (17)]. $\Delta t_{\min}$ is very small compared to the period of the input waveforms of usual interest, i.e.,

$$\Delta t_{\min} \ll 2\pi/\omega \tag{2b}$$

where ω is the input frequency.

Sinusoidal-Input Describing Function (DF) for the Pseudorate Controller

The steady-state operation of the dual time constant feedback lag network pseudorate (Fig. 1), in response to a sinusoidal input $f(t) = A\sin\omega t$, is depicted in Fig. 2. The $y(t)$, $a(t)$, and $e(t)$ waveforms are symmetric, periodic, and zero mean, in accordance with the form of the input and the symmetry of the hysteresis switch with its feedback. The pseudorate is assumed to have turned on at times $t_1, t_2, \ldots, t_n$ and off at times $t_1+\Delta t_1, t_2+\Delta t_2, \ldots, t_n+\Delta t_n$. If $y(t)=0$, turn-on occurs when

$$A\sin\omega t_i - a(t_i) = D \tag{3}$$

where

$$a(t_i) = a(t_{i-1}+\Delta t_{i-1})\exp\{-[t_i-(t_{i-1}+\Delta t_{i-1})]/\tau_f\} \tag{4}$$

and $i=2,\ldots,n$. The condition of periodicity of $a(t)$ necessitates that $a(t_1) = -a(\pi/\omega + t_1)$ or, equivalently,

$$a(t_1) = -a(t_n+\Delta t_n)\exp\{-[\pi/\omega + t_1 - (t_n+\Delta t_n)]/\tau_f\} \tag{5}$$

If $y(t) = \pm 1$, turn-off occurs when

$$a\sin\omega(t_i+\Delta t_i) - a(t_i+\Delta t_i) = D-H \tag{6}$$

where $i=1,2,\ldots,n$, and

$$a(t_i+\Delta t_i) = K_fD[(1-\exp(-\Delta t_i/\tau_0)] + a(t_i)\exp(-\Delta t_i/\tau_0) \tag{7}$$

For a given integer n, the preceding expressions contain $2n$ constants $a(t_i)$ and $a(t_i+\Delta t_i)$ and $2n$ unknown values of t_i and Δt_i. (A and ω are viewed as known inputs.) Equations (4, 5, and 7) may be manipulated to obtain expressions for $a(t_i)$ and $a(t_i+\Delta t_i)$ in terms of unknowns t_i and Δt_i; the results then may be combined with Eqs. (3) and (6) to eliminate the $a(t)$'s and obtain $2n$ transcendental equations to be solved for the $2n$ unknowns t_i and Δt_i.

The describing function[9] then can be calculated via

$$N(A,\omega) = (1/A)(b_1 + ja_1) \tag{8}$$

where

$$a_1 = \frac{2}{\pi}\sum_{i=1}^{n}[\sin\omega(t_i+\Delta t_i) - \sin\omega t_i]$$

$$b_1 = \frac{2}{\pi}\sum_{i=1}^{n}[\cos\omega t_i - \cos\omega(t_i+\Delta t_i)]$$

For values of n other than 1, generating the describing function is necessarily numerical and complicated by the fact that n generally is not known in advance.

For the problem at hand, where the input sinewave amplitude of interest is near the deadband (only small values of n are of concern) and the frequencies of interest are either well within the system bandwidth (such as the rigid vehicle limit cycle) or well outside it (such as the flexible mode frequency $\omega_1 \gg 1/\tau_f$), the process of obtaining the describing function can be simplified. For $n=1$, an analytic expression for the describing function can be obtained. Detailed analysis of the system, using a describing function based on the $n=1$ assumption, uncovers the fundamental relationships that govern the near-deadband pseudorate control of flexible vehicles and provides a basis for understanding the system's behavior when $n=2, 3, \ldots$, etc.

Exact DF ($n=1$)

For $n=1$, Eqs. (5) and (7) combine to give

$$a(t_1) = \frac{-K_fDJ(\omega)[\exp(\Delta t_1/\tau_f) - \exp(-\Delta t_1/\tau)]}{1+J(\omega)\exp(-\Delta t_1/\tau)} \tag{9}$$

and

$$a(t_1+\Delta t_1) = K_fD[1-\exp(-\Delta t_1/\tau_0)] + a(t_1)\exp(-\Delta t_1/\tau_0) \tag{10}$$

where

$$J(\omega)=\exp(-\pi/\omega\tau_f) \quad \text{and} \quad \tau=\tau_0\tau_f/(\tau_f-\tau_0)$$

Substitution of Eq. (9) into Eq. (3) and rearrangement gives

$$A\sin\omega t_1 - D + K_f D J(\omega)\exp(\Delta t_1/\tau_f) + J(\omega)[A\sin\omega t_1 - D(K_f+1)]\exp(-\Delta t_1/\tau) = 0 \quad (11)$$

Substitution of Eq. (9) into (10), then substitution of the result into Eq. (6), and then arrangement gives

$$A\sin\omega(t_1+\Delta t_1) - \phi_s + K_f D\exp(-\Delta t_1/\tau_0) + J(\omega)[A\sin\omega(t_1+\Delta t_1) - (D-H)]\exp(-\Delta t_1/\tau) = 0 \quad (12)$$

where the saturation angle is defined as $\phi_s = K_f D + D - H$. Equations (11) and (12) constitute a pair of transcendental equations which, for a given A and ω, can be solved numerically for t_1 and Δt_1. The DF then is calculated by Eq. (8).

Approximate DF ($n=1$)

For the pseudorate as described via Eqs. (1) and (2) (i.e., Δt_1 assumed to be of the order of $\Delta t_{\min}$), the following approximations linear in Δt_1 are valid:

$$\exp(-\Delta t_1/\tau_0) = 1 - \Delta t_1/\tau_0; \quad \exp(\Delta t_1/\tau_f) = 1 + \Delta t_1/\tau_f \quad (13)$$

$$\sin\omega(t_1+\Delta t_1) = \sin\omega t_1 + \omega\Delta t_1\cos\omega t_1 \quad (14)$$

Substitution of Eq. (13) into Eq. (11) and rearrangement yields, to linear order in Δt_1,

$$A[1+J(\omega)(1-\Delta t_1/\tau)]\sin\omega t_1 + J(\omega)D\Delta t_1[K_f/\tau_f + (K_f+1)/\tau] - D[1+J(\omega)] = 0 \quad (15)$$

Similarly, substitution of Eqs. (13) and (14) into Eq. (12) and rearrangement gives

$$A[1+J(\omega)(1-\Delta t_1/\tau)]\sin\omega t_1 - \Delta t_1\{K_f D/\tau_0 - J(\omega)(D-H)/\tau - A\omega[1+J(\omega)]\cos\omega t_1\} - [1+J(\omega)](D-H) = 0 \quad (16)$$

Subtraction of Eq. (15) from Eq. (16) and solution for Δt_1 yields

$$\Delta t_1 = \frac{H}{K_f D/\tau_0 + J(\omega)H/[1+J(\omega)]\tau - A\omega\cos\omega t_1} \quad (17)$$

Substitution of Eq. (17) into Eq. (15) yields

$$\sin\omega t_1 = \frac{D}{A}\left[1 - \frac{J(\omega)}{1+J(\omega)}\left(\frac{K_f}{\tau_0}+\frac{1}{\tau}\right)\Delta t_1\right] \quad (18)$$

Since $J(\omega)$ varies from 0 to 1 as ω increases from zero, $J(\omega)/[1+J(\omega)]$ varies from 0 to ½ over the same frequency range. From Eqs. (17) and (2), one concludes that the assumption that Δt_1 is of the order of $\Delta t_{\min}$ is valid. Therefore, Eqs. (17) and (18) reduce to

$$\Delta t_1 \simeq H\tau_0/K_f D \quad (19)$$

$$t_1 \simeq \frac{1}{\omega}\sin^{-1}\left[\frac{1}{A}\left\{D - \frac{J(\omega)}{1+J(\omega)}H\right\}\right] \quad (20)$$

Linear approximations in Δt_1 of the type introduced in Eq. (14) enable approximation of a_1 and b_1 of Eq. (8) by $(2\omega\Delta t_1/\pi)\cos\omega t_1$ and $(2\omega\Delta t_1/\pi)\sin\omega t_1$, respectively. Furthermore, conversion to polar form leads to the approximate expression for the DF:

$$N(A,\omega) = (2\omega\Delta t_1/\pi A)\exp[-j(\pi/2-\omega t_1)] \quad (21)$$

Equation (21) illustrates the inherent "lead" characteristic of the pseudorate circuit, since ωt_1 is never greater than $\pi/2$. In Eq. (21), Δt_1 and t_1 can be viewed as given by solution of the transcendental Eqs. (17) and (18) or given directly (but in a more approximate way) by Eqs. (19) and (20).

Equations (11) and (12) and their subsequent approximations are based on the assumption that the input sinewave amplitude A is such that $n=1$ for all frequencies ω of interest. For a given pseudorate, the input sinewave amplitude range for which $n=1$ (or $n=2$, 3, ..., etc., for that matter) is determined most easily by simulation. However, some guidelines are evident. A lower bound on A (below which pulsing in response to a sinusoidal input ceases) is given by [see Eq. (20)].

$$A > D - \{J(\omega)/[1+J(\omega)]\}H \quad (22)$$

Analysis of the waveforms of Fig. 2 leads to the conclusion that an upper bound on A (for $n=1$) is defined via the condition

$$A < D + a(\pi/2\omega) \quad (23)$$

where

$$a(\pi/2\omega) = a(t_1+\Delta t_1)\exp\{-(\pi/2\omega - [t_1+\Delta t_1])/\tau_f\}$$

Combining Eqs. (9, 10, and 23) and the linear approximations in Δt_1 results in the following upper bound on A for $n=1$:

$$A < D + \{J(\omega)/[1+J(\omega)]\}H\exp[-(\pi/2\omega - t_1)/\tau_f] \quad (24)$$

For low ω (for small $\omega\tau_f$, i.e., for the rigid vehicle limit cycle frequency), $J(\omega)$ is very small, and hence A must be very close to D if n is to be unity. For the higher frequency range of interest (flexible mode, $\omega\tau_f \gg 1$), $J(\omega)\simeq 1$, and the input sinewave amplitude range is bounded by

$$D - H/2 < A < D + H/2 \quad (25)$$

Approximate DF ($n=2,3$, etc.)

A DF covering the flexible mode frequency range ($\omega \gg \omega_b$) and having amplitudes greater than $D+H/2$ (n greater than unity) is of interest. Such a DF determination is complicated by the fact that, for a given A and ω, the appropriate n must be determined, along with t_i and Δt_i, $i=1, 2, \ldots, n$. Various approximations can be made which simplify the mechanics of generating the DF; the set on which the results presented in this paper are based is derived below.

Where $\omega\tau_f$ is sufficiently large, exponential functions with τ_f in the argument can be approximated by unity. With this approximation and Eqs. (13) and (14), and proceeding in the manner outlined in Eqs. (13-18), one can derive counterparts of Eqs. (17) and (18) for the case when n is arbitrary:

$$\Delta t_i = \frac{H}{K_f D/\tau_0 - A\omega\cos\omega t_i} \quad (26)$$

$$\sin\omega t_i = \frac{D}{A}\left[1 - \frac{K_f}{\tau_0}\left\{\frac{1}{2}\sum_{k=1}^{n}\Delta t_k - \sum_{k=1}^{i-1}\Delta t_k\right\}\right] \quad i=1,2,\ldots n \quad (27)$$

By noting the mechanics of the pseudorate behavior, it becomes evident that the last (nth pulse always occurs before

Table 1 Typical CTS parameter values

Parameter	Description	Value	Units
D	Deadband	0.1632	deg
H	Hysteresis	0.0223	deg
$K_f D$	Feedback lag network gain	2.964	deg
τ_0	On-time constant	2.084	s
τ_f	Off-time constant	39.6	s
F	Thrust level	0.242	lbf
L	Moment arm	2.07	ft
I	Spacecraft inertia (flexible + rigid)	822.4	slug-ft^2
k_1	Modal gain: first flexible mode	7.7	...
ρ_1	Modal damping factor: first flexible mode	0.003-0.008	...
ω_1	Modal frequency: first flexible mode	1.9-2.3	rad/s
K	Attitude sensor gain	1	...
T	Loop time delay	0-1.25	s
$\Delta t_{\min}$	Minimum on-time	15.71	ms
ϕ_s	Pseudorate saturation angle	3.105	deg

Table 2 Approximate DF on-off times as a function of input sinewave amplitude

n	Input sinewave amplitude range, deg	$a(t)_{\max}$ $nH/2$, deg	t_1, s	Δt_1, ms	t_2	Δt_2	t_3	Δt_3	t_4	Δt_4	t_5	Δt_5
1	0.1521-0.1744	0.01115	0.810 -0.559	15.68	...	...	...	...	...	...	...	...
2	0.1744-0.1855	0.0223	0.492 -0.455	15.68	0.632 -0.569	15.68	...	...	...	...	...	...
3	0.1855-0.1967	0.03345	0.406 -0.381	15.68	0.504 -0.467	15.68	0.640 -0.577	15.68	...	...	...	...
4	0.1967-0.2078	0.0446	0.340 -0.321	15.68	0.419 -0.394	15.68	0.514 -0.480	15.68	0.646 -0.585	15.68	...	...
5	0.2078-0.2190	0.0669	0.285 -0.270	15.68	0.354 -0.334	15.68	0.431 -0.404	15.68	0.523 -0.485	15.68	0.652 -0.587	15.68

Table 3 Simulated pseudorate steady-state on-off times as a function of input sinewave amplitude

n	Input sinewave amplitude range, deg	$a(t)_{\max}$ $nH/2$, deg	t_1, s	Δt_1, ms	t_2	Δt_2	t_3	Δt_3	t_4	Δt_4	t_5	Δt_5
1	0.152-0.173	0.0117 -0.0126	0.780 -0.556	16.9 -18.1	...	...	...	...	...	...	...	...
2	0.174-0.184	0.0262	0.477 -0.443	19.3	0.653 -0.584	18.1	...	...	...	...	...	...
3	0.185-0.198	0.0388 -0.0405	0.389 -0.356	19.3 -20.5	0.508 -0.459	19.3	0.698 -0.593	16.9 -18.1	...	...	...	...
4	0.198-0.210	0.0537 -0.0549	0.309 -0.289	20.5	0.410 -0.382	19.3 -20.5	0.528 -0.492	19.3	0.720 -0.637	16.9 -18.1	...	...
5	0.213-0.220	0.0678 -0.0715	0.245 -0.227	21.8	0.337 -0.314	20.5 -21.8	0.430 -.0411	20.5	0.557 -0.520	19.3	0.785 -0.673	16.9 -18.1

the point in the periodic cycle at which the magnitude of the function, $A\sin\omega t$, starts to diminish. That is, n is the maximum integral number for which

$$\omega t_n \leq \pi/2 \tag{28}$$

The transcendental Eqs. (26-28) may be solved to determine the Δt_i, t_i, and n.

A first-order approximation for Δt_i may be deduced from Eq. (26) to be a constant, Δt, given by

$$\Delta t \simeq H\tau_0/K_f D \tag{29}$$

A corresponding direct formula for the integer n, deduced from Eqs. (27-29), is

$$n = \text{integer part of } [2(A+H-D)/H] \tag{30}$$

A corresponding approximate value for t_i then is found from Eq. (27) to be

$$t_i = (1/\omega)\sin^{-1}[(1/A)\{D+(i-1)H-\tfrac{1}{2}nH\}] \tag{31}$$

Also, one may deduce the following input sinewave amplitude range for a given $n = 2, 3...$ [a counterpart of Eq. (25)]:

$$D+(n-1)H/2 < A < D+nH/2 \tag{32}$$

The coefficients of the describing function which correspond to Eqs. (29-32) are found to be

$$b_1 = \frac{2\omega\Delta t}{\pi}\sum_{i=1}^{n}\sin\omega t_i \qquad a_1 = \frac{2\omega\Delta t}{\pi}\sum_{i=1}^{n}\cos\omega t_i \tag{33}$$

Equations (29-33) yield a reasonably accurate DF provided that $n < \sim 5$. Results given in this paper for $n > 1$ are based on these equations. The DF can be calculated more accurately where required by solving Eqs. (26-28) via an iterative (relaxation) type of solution, with Eqs. (29-31) used as the starting solution.

Confirmation of DF Formula

Pseudorate parameter values characteristic of the CTS are given in Table 1. The magnitude and phase of the exact DF for $n=1$, as obtained after solving Eqs. (11) and (12) by a Newton-Raphson technique, are shown in Fig. 3. The input amplitude ranges and the t_i and Δt_i for the approximate DF for $n<5$ and $\omega \gg 1/\tau_f$ are shown in Table 2. For example, Table 2 indicates that, when the input sinewave amplitude is in the range 0.1521 to 0.1744 deg, then $n=1$, Δt_1 is constant at 15.68 ms, and t_1 has values between 0.810 and 0.559 s. Table 3 summarizes the corresponding sinusoidal response characteristics obtained via digital simulation. Comparison of Tables 2 and 3 shows that amplitude ranges and switching times involved in the calculation of the approximate DF using Eqs. (29-33) are in keeping with the results obtained via simulation.

Rigid Vehicle Mode Limit Cycle Investigation

In the absence of flexibility (setting $k_1 = 0$ in Fig. 1), the transfer function for the dynamics and attitude sensor is

$$G(\omega) = -KFL\, e^{-j\omega T}/I\omega^2 \tag{34}$$

From the approximate expression for the DF when $n=1$ [Eq. (21)] we have

$$-1/N(A,\omega) = -\pi A \exp[-j(\pi/2 - \omega t_1)]/2\omega\Delta t_1 \tag{35}$$

where Δt_1 and ωt_1 are given in Eqs. (19) and (20), respectively. Equating $-1/N(A,\omega)$ and $G(\omega)$ gives

$$\omega_{LR}(t_{1LR} + T) = \pi/2 \tag{36}$$

$$\omega_{LR} = 2KFL\Delta t_{1LR}/\pi I A_{LR} \tag{37}$$

where the subscript LR denotes rigid vehicle limit cycle. Since the time delay T of interest here is comparable with the period of the flexible mode which has a frequency well outside the rigid vehicle system bandwidth (i.e., $\omega_1 \gg \omega_b$), it follows that $T \ll t_{1LR}$. Equation (36) thus reduces to $\omega_{LR} t_{1LR} = \pi/2$, which, in conjunction with Eq. (2), implies that $A_{LR} = D$. From Eq. (1e) and the fact that $J(\omega) = \exp(-\pi/\omega\tau_f)$, it is apparent that $J(\omega) \ll 1$ for frequencies (such as ω_{LR}) which are inside the rigid vehicle closed-loop bandwidth ω_b. Substituting $\Delta t_{1LR} = H\tau_0/K_f D$ and $A_{LR} = D$ into Eq. (37) results in the following expressions for the rigid vehicle limit cycle amplitude and frequency:

$$A_{LR} = D \qquad \omega_{LR} = 2KFL(H\tau_0/\pi I K_f D^2) \tag{38}$$

The stability of the predicted limit cycle can be determined by evaluating the partial derivatives (at A_{LR}, ω_{LR}) involved in Loeb's criterion for stability, which is[9]

$$\frac{\partial U}{\partial A}\frac{\partial V}{\partial \omega} - \frac{\partial U}{\partial \omega}\frac{\partial V}{\partial A} > 0 \tag{39}$$

where U and V are the real and imaginary parts of the characteristic equation, $1 + N(A,\omega)G(\omega) = 0$. For the case at hand, Eq. (39) reduces to

$$D/(\omega_{LR} A_{LR} \cos\omega_{LR} t_{1LR}) - \omega_{LR} T > 0 \tag{40}$$

which indicates that the $n=1$ type of rigid vehicle limit cycle is stable for the small time delays of interest.

Flexible Mode Limit Cycle Analysis

By closing the loop through the flexible mode only of Fig. 1, the transfer function for the dynamics and attitude sensor is

$$G(\omega) = [KFLk_1/I\omega_1^2 F(\omega)] \exp\{-j[\sigma(\omega) + \omega T]\} \tag{41}$$

where

$$F(\omega) = [\{1 - (\omega/\omega_1)^2\}^2 + (2\rho_1\omega/\omega_1)^2]^{1/2}$$

$$\sigma(\omega) = \tan^{-1}[(2\rho_1\omega/\omega_1)/\{1 - (\omega/\omega_1)^2\}]$$

Confining our attention for the moment to a search for $n=1$ type of limit cycles in the flexible mode frequency range, we have $J(\omega) \simeq 1$ and hence, from Eq. (20),

$$\omega t_1 \simeq \sin^{-1}[(D - H/2)/A] \tag{42}$$

For $n=1$, the input amplitude (limit cycle amplitude) range is restricted to that given in Eq. (25). Equating magnitude and phase components of $-1/N(A,\omega)$ in Eq. (35) and $G(\omega)$ in Eq. (41) gives

$$KFLk_1/I\omega_1^2 F(\omega) = \pi A/2\omega\Delta t_1 \tag{43}$$

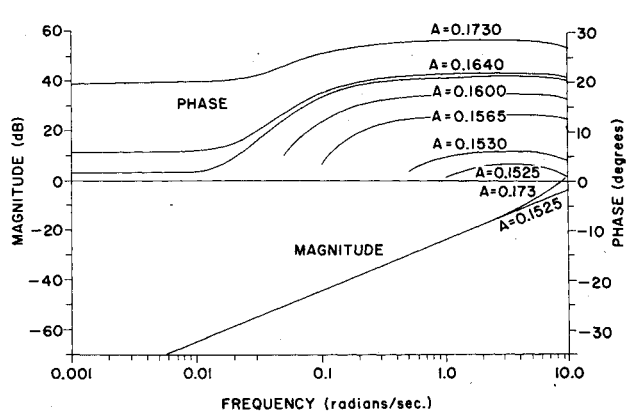

Fig. 3 Magnitude and phase of exact describing function ($n=1$, no restriction on ω).

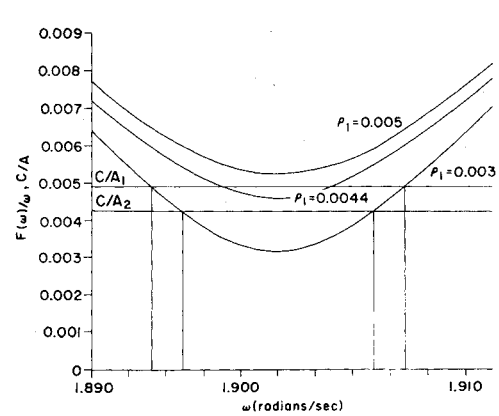

Fig. 4 $F(\omega)/\omega$ and C/A as a function of ω for selected ρ_1 ($n=1$, flexible mode only).

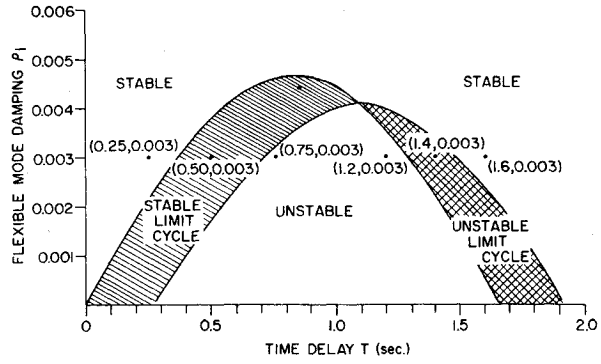

Fig. 5 Flexible mode stability as a function of ρ_1 and $T(n=1, A_1<A<A_2)$.

$$\sigma(\omega)+\omega T=3\pi/2-\omega t_1 \tag{44}$$

which must be solved subject to the constraint given in Eq. (25) to obtain A_{LF} and ω_{LF}. Whether Eqs. (43) and (44) have a solution or not depends on (among other parameters) the time delay T and the modal damping ρ_1. It is convenient to write Eq. (43) in the form

$$F(\omega)/\omega=C/A \tag{45}$$

where $C=2KFLk_1\Delta t_1/\omega_1^2\pi$. For a given D, H, C, and ω_1, a plot of the left-hand side and the right-hand side of Eq. (45) vs ω (in the range of ω_1 and for selected ρ_1) produces curves such as those shown in Fig. 4. Since A is restricted to the range indicated in Eq. (25) (that is, between $A_1=D-H/2$ and $A_2=D+H/2$ as depicted in Fig. 4), then there are only certain values of ω (if any) for which Eq. (45) is applicable. It is seen from Fig. 4 that there are three possible cases:

1) There is no solution (illustrated by the $\rho_1=0.005$ curve).

2) There is one range of solution (illustrated by the $\rho_1=0.0044$ curve).

3) There are two solution ranges (illustrated by the $\rho_1=0.003$ curve).

The values of ρ_1 above which limit cycles are not predicted (case 1) is obtained by setting $\omega=\omega_1$ and $A=A_1$ in Eq. (45). The condition is

$$\rho_1>KFL\Delta t_1/[\pi\omega_1\{D-H/2\}] \tag{46}$$

that is, when the modal damping is greater than the quantity on the right-hand side of Eq. (46), DF theory says that it is not possible for an $n=1$ type of limit cycle to exist, irrespective of what time delay is present.

For lower values of ρ_1, the frequency range (ranges) over which Eqs. (25) and (45) are satisfied (cases 2 and 3) can be read directly off the graph (Fig. 4). From Eq. (44), the corresponding time delays are calculated via

$$T=(1/\omega)[3\pi/2-\sin^{-1}[(D-H/2)/A]-\sigma(\omega)] \tag{47}$$

Plotting the time delays calculated in this manner as a function of damping (for the modal frequency ρ_1 indicated in Fig. 4) results in the stability boundaries indicated in Fig. 5. The shaded areas indicate the ranges of time delay and modal damping for which $n=1$ type of limit cycles are possible. That is, the shaded areas indicate the ranges of T and ρ_1 for which Eqs. (43) and (44) have a solution $[A_{LR}, \omega_{LR}]$ such that $A_1<A_{LF}<A_2$.

For a given point (T, ρ_1) in the shaded area of Fig. 5, the actual limit cycle solution $[A_{LF}, \omega_{LF}]$ is found readily by plotting the real and imaginary parts of $N(A,\omega)G(\omega)$ [where $N(A,\omega)$ is given in Eq. (21), and $G(\omega)$ is given in Eq. (41)] as a function of ω for $A_1<A<A_2$, and reading A_{LF} and ω_{LF} from the curve that intersects the $-1+j0$ point in the

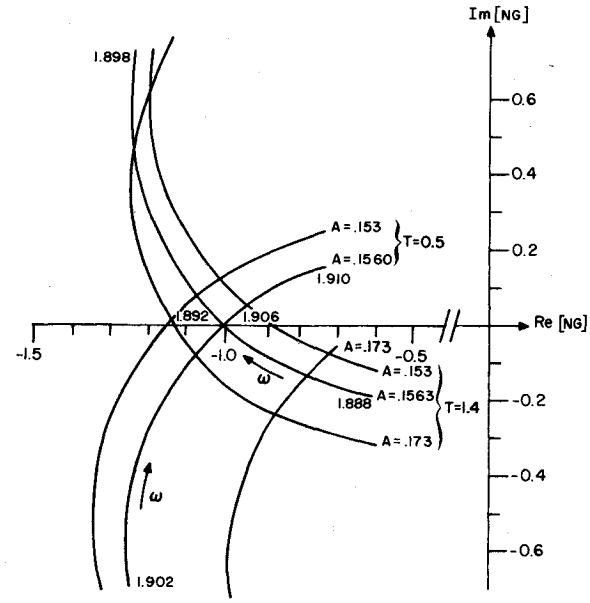

Fig. 6 Limit cycle determination when $T=0.5$, 1.4 s ($n=1$, flexible mode only).

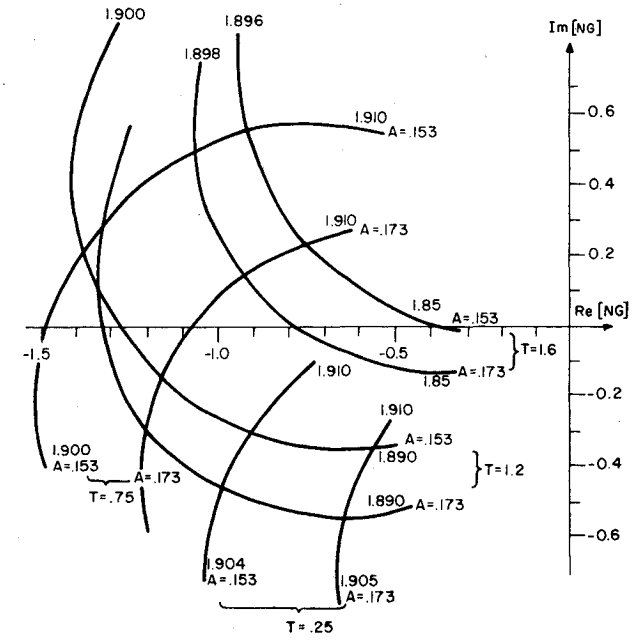

Fig. 7 Real and imaginary parts of $N(A,\omega)G(\omega)$ for $T=0.25$, 0.75, 1.2, and 1.6 s ($n=1$, flexible mode only).

$N(A,\omega)G(\omega)$ plane. The technique is illustrated in Fig. 6 for the (0.50,0.003) and (1.4,0.003) points taken from the shaded areas in Fig. 5. The corresponding limit cycle solutions are (0.156 deg, 1.904 rad/s) and (0.1563 deg, 1.893 rad/s), respectively. Numerically evaluating the partial derivative in Loeb's criterion [Eq. (39)] indicates that the former limit cycle is stable and the latter is unstable. That is, the shaded area on the left in Fig. 5 is a stable limit cycle region, and the shaded area on the right is an unstable limit cycle region.

For points (T,ρ_1) not in the shaded areas of Fig. 5, no limit cycles exist; however, the flexible mode behavior is predicted readily by plotting the real and imaginary parts of $N(A,\omega)G(\omega)$ as a function of ω (for the limiting amplitudes A_1 and A_2 only) and invoking the Nyquist encirclement criteria to determine stability. The technique is illustrated in Fig. 7 for several (T, ρ_1) pairs outside the shaded area indicated in Fig. 5. The (0.75, 0.003) and (1.2, 0.003) points in Fig. 5 result in a set $(A_1<A<A_2)$ of Nyquist curves (Fig. 7)

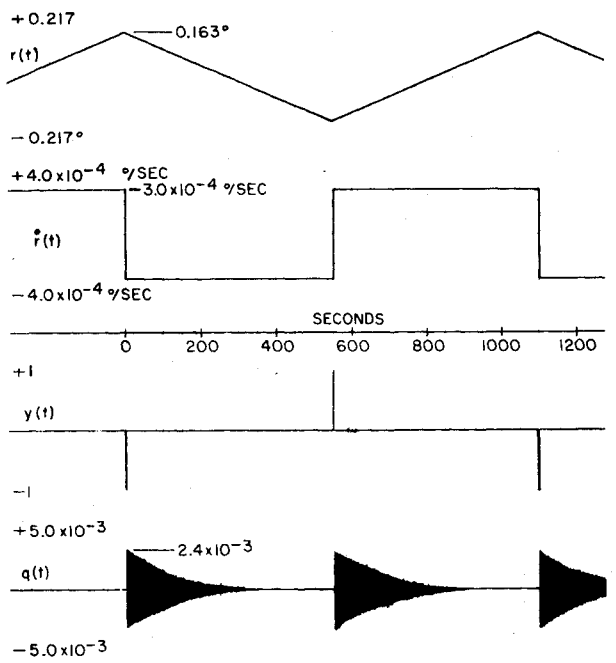

Fig. 8 Low-frequency rigid vehicle limit cycle.

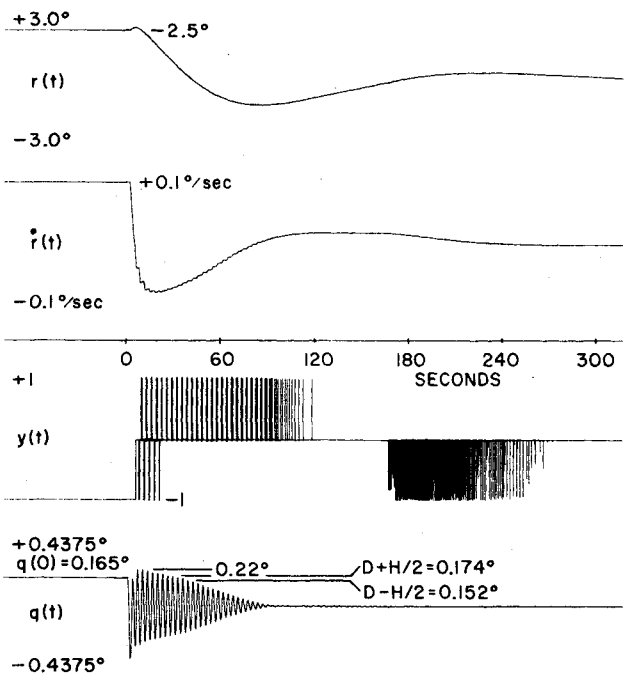

Fig. 9 Initial condition response, $T=0.28$ s [$r(0)=2.5$ deg, $\dot{r}(0)=0.1$ deg/s, $q(0)=0.165$ deg, $\dot{q}(0)\times=0$ deg/s].

that encircle the $-1+j0$ point. Thus, when the time delay and modal damping are such that (T, ρ_1) is located below the shaded area of Fig. 5, the flexible mode initial condition response to amplitudes between A_1 and A_2 is unstable in the sense that it diverges in amplitude to the point where A_2 is exceeded. The same can be said about the unstable limit cycle area (the shaded area on the right) of Fig. 5. On the other hand, the (0.25, 0.003) and (1.6, 0.003) points in Fig. 5 result in a set of Nyquist curves (Fig. 7) that do not encircle the $-1+j0$ point. Thus, when the time delay and modal damping are such that (T, ρ_1) is located above the shaded area of Fig. 5, the flexible mode initial condition response to amplitudes between A_1 and A_2 is stable in the sense that it decays to zero.

To this point, we have restricted our attention to the flexible mode behavior when $A_1<A<A_2$, i.e., when $n=1$. As

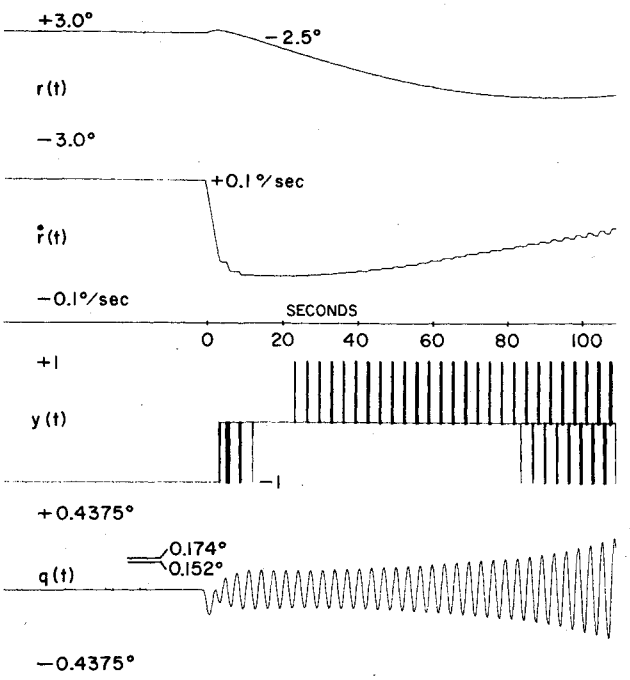

Fig. 10 Initial condition response, $T=0.75$ s [$r(0)=2.5$ deg, $\dot{r}(0)=0.1$ deg/s, $q(0)=0$ deg, $\dot{q}(0)=0$ deg/s].

summarized in Fig. 5, it is evident that the $n=1$ stability behavior is determined by T and ρ_1. For larger amplitudes (i.e., $n>1$ but $n<5$), Fig. 5 theoretically does not apply; however, it is indicative of the type of behavior which can be expected. Nyquist curves (not shown) when $n=2,3,\ldots$ using the approximate DF of Eqs. (29-33) indicate that the stable and unstable regions of Fig. 5 remain effectively unchanged when $n=2,3,\ldots$.

Simulation Results

The foregoing limit cycle and stability analysis is confirmed readily by hybrid and digital computer simulation of the system shown in Fig. 1. Simulation with the flexible mode only (i.e., the $1/s^2$ path of Fig. 1 disconnected) yields results that are in complete accord with material presented in Figs. 4-7. Such simulation results do not reveal anything new and so, in the interest of brevity, are not included.

Simulation with the rigid spacecraft [i.e., the flexible mode absent $(k_1=0)$] indicates that the system has a reasonable large-angle [$r(0)=2.5$ deg, $\dot{r}(0)=0.1$ deg/s] rigid vehicle initial condition response in accordance with the design criteria placed on the system and that the response converges to the low-frequency deadband-to-deadband type of limit cycle, as shown in strips 1, 2, and 3 of Fig. 8. The observed rigid vehicle limit cycle frequency is 0.0028 rad/s (period of 2200 s). The corresponding frequency given by Eq. (38) is 0.0022 rad/s (period of 2800 s). The difference is because Eq. (38) is based on the assumption that the limit cycle is sinusoidal, whereas in reality it is triangular. Furthermore, small time delays of the magnitude considered in this paper have no effect on the rigid vehicle response or the rigid vehicle limit cycle frequency.

Of prime concern here is the behavior of the system when both rigid and flexible modes are present and how well the mode separation/single input DF technique predicts this behavior. The simulation results presented in Fig. 8-10 pertain to this situation. In all cases, the periods of the rigid vehicle limit cycle and the flexible mode vibration are 2200 and 3.3 s, respectively.

Figure 8 illustrates the low-frequency deadband-to-deadband limit cycle behavior and stable flexible mode behavior when both modes are included in the spacecraft dynamics. Once in this state, the flexible mode can jeopardize

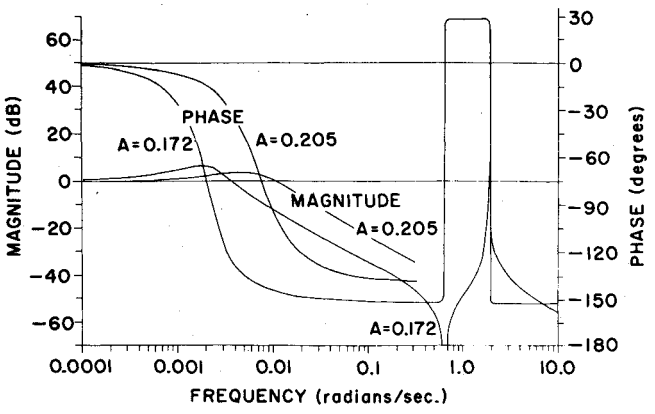

Fig. 11 Closed-loop frequency response, $X(\omega)/U(\omega)$ with the pseudorate controller replaced by $N(A,\omega)$.

stability only if the parameters are such that T and ρ_f constitute a point pair in the unstable areas of Fig. 5 *and* external disturbances are present which significantly increase the flexible mode output over that shown in strip 4 of Fig. 8. In the absence of external perturbations, structural flexibility and small loop time delays have no effect on the low-frequency limit cycle, and Eq. (38) approximately describes the situation.

Figures 9 and 10 show two initial condition responses when both modes are present, $\rho_f = 0.003$, and the loop time delay is 0.28 and 0.75 s, respectively. In accordance with the preceding sections, it is expected that, for the $T = 0.28$ s case, the flexible mode response will (if excited) decay to zero and that the system response will converge to the low-frequency rigid vehicle limit cycle. For the $T = 0.75$ s case, it is expected that the flexible mode will, if sufficiently excited, diverge and dominate the system response. Figures 9 and 10 show that this is, indeed, the case.

Concluding Remarks

The mode separation/single input describing function technique illustrated in this paper facilitates analysis of the system shown in Fig. 1. Only near-deadband operation is considered, and the two modes (a rigid vehicle mode and a highly underdamped mode due to structural flexibility) are well separated in frequency. Analysis of the effect of the controller on the stability of each dynamical mode individually allows accurate predictions to be made concerning the stability of such a multimode system. A rigid vehicle stable limit cycle dominates the low-frequency response behavior, and a decaying or divering flexible mode response dominates the high-frequency behavior of the system.

If the loop time delay and modal damping are such that the Nyquist criteria indicate stable flexible mode behavior, then the flexible mode response decays to zero, and the low-frequency rigid vehicle limit cycle ultimately dominates the system response. If the flexible mode damping factor is above the critical value given in Eq. (46), the flexible mode response will decay to zero irrespective of the loop time delay.

For other values of loop time delay and modal damping, the Nyquist criteria indicate unstable flexible mode behavior. In these cases, a divergent flexible mode response (if flexible mode is excited) dominates the system behavior (dominates the low-frequency rigid vehicle limit cycle), and system stability is jeopardized. To avoid such behavior, either the structure should be designed to have a structural damping factor greater than that given by the right-hand side of Eq. (46) or the pseudorate parameters must be selected so that Eq. (46) is well satisfied.

The stable flexible mode limit cycles predicted via the Nyquist criteria (in the absence of the rigid vehicle mode) for certain values of delay and modal damping are of limited practical significance. The symmetrical limit cycle predicted is destroyed readily when both modes are present in the loop. In keeping with the sharp amplitude and phase shifts associated with highly underdamped modes, the results are very sensitive to changes in T, ρ_f, and ω_f.

The analysis approach illustrated in this paper (mode separation/single input DF technique) is expected to be applicable to a wide range of nonlinear controller/flexible vehicle combinations. Whether or not the mode separation technique applies in any particular situation involves engineering judgment. The fact that the modes in our example are well separated in frequency is seen in Fig. 11, where the pseudorate controller in Fig. 1 is replaced by its describing function $N(A,\omega)$, and the closed-loop frequency response for the resulting system is plotted for two different values of A. The flexible mode frequency is seen to be well outside the rigid vehicle system bandwidth. From another point of view, the fact that the modes are well separated in frequency here means that, for low frequencies, the spacecraft dynamics transfer function $G(\omega) = X(\omega)/Y(\omega)$ (see Fig. 1) reduces to the $G(\omega)$ given in Eq. (34) and that, for high frequencies ($\omega \simeq \omega_f$), the spacecraft dynamics transfer function reduces to the $G(\omega)$ given in Eq. (41).

Acknowledgments

The authors wish to acknowledge the dedicated efforts of D.L. Wood in generating the digital programs, the graphs, and the hybrid computer runs illustrated in this paper.

References

[1] Franklin, C.A. and Davidson, E.H., "A High-Power Communications Technology Satellite for the 12 and 14 GHz Bands," *AIAA Progress in Astronautics and Aeronautics: Communications Satellite Systems,* edited by P.L. Bargellini, Vol. 32, New York, 1973, pp. 87-121.

[2] Vigneron, F.R., McMillan, D.V., and Kettlewell, J.R., "The Attitude Stabilization and Control System for the Communications Technology Satellite," *NTC '72 Record, 1972 National Telecommunications Conference,* Houston, Texas, IEEE Pub. 72 CH0601-5-NTC, Dec. 4-6, 1972.

[3] Porcelli, G., "Attitude Control of Flexible Space Vehicles," *AIAA Journal,* Vol. 10, June 1972, pp. 807-812.

[4] Greensite, A.L., *Analysis and Design of Space Vehicle Flight Control Systems, Control Theory,* Vol. II, Spartan Books, New York, 1970, pp. 305-316, 345.

[5] Gevarter, W.B., "Basic Relations For Control of Flexible Vehicles," *AIAA Journal,* Vol. 8, April 1970, pp. 666-672.

[6] Millar, R.A. and Vigneron, F.R., "The Effect of Structural Flexibility on the Stability of Pitch for the Communications Technology Satellite," *Proceedings of the 1975 Canadian Conference on Automatic Control,* Univ. of British Columbia, Vancouver, B.C., Canada, June 23-24, 1975.

[7] Hughes, P.C., "Dynamics of Flexible Space Vehicles with Active Attitude Control," *Celestial Mechanics,* Vol. 9, March 1974, pp. 21-39.

[8] Scott, E.D., "Pseudorate Sawtooth-Pulse-Reset Control System Analysis and Design," *Journal of Spacecraft and Rockets,* Vol. 4, June 1967, pp. 781-785.

[9] Gelb, A. and Vander Velde, W.S., *Multiple-Input Describing Functions and Non-Linear System Design,* McGraw-Hill, New York, 1968, pp. 52-55, 121.